Acta Biomaterialia 213 (2026) 328–340

Contents lists available at ScienceDirect

Acta Biomaterialia

journal homepage: www.elsevier.com/locate/actbio

Full length article

Exploring the link between disturbed flow and endothelial cell function in an *in vitro* arteriovenous fistula model

Zhuotao Xiao [a,b], Nicholas A. White [a,c], Jun Wen [d], Rudmer J. Postma [a], Wendy M.P.J. Sol [a], Bernard M. van den Berg [a], Anton Jan van Zonneveld [a], Huybert J.F. van de Stadt [e], Asad Mirza [f], Roel Bijkerk [a], Joris I. Rotmans [a,*]

[a] *Department of Internal Medicine (Nephrology) and the Einthoven Laboratory for Vascular and Regenerative Medicine, Leiden University Medical Center, Leiden 2333, ZA, Netherlands*
[b] *Department of Nephrology, The First Affiliated Hospital of Soochow University, Suzhou 215000, China*
[c] *Department of BioMechanical Engineering, Delft University of Technology, Delft 2628, CN, Netherlands*
[d] *Department of Computer Science and Technology, Southwest University of Science and Technology, Mianyang 621010, China*
[e] *Department of Medical Technology, Design & Prototyping, Leiden University Medical Center, Leiden 2333, ZA, Netherlands*
[f] *Department of Biomedical Engineering, Florida International University, Miami, FL, 33199, United States*

ARTICLE INFO

Keywords:
Arteriovenous fistulas
Disturbed flow
In vitro model
Computational fluid dynamics
Hemodynamics

ABSTRACT

Background: The disturbed flow contributes to juxta-anastomotic intimal hyperplasia (IH) in arteriovenous fistulas (AVFs). This study developed an *in vitro* method aiming to understand the hemodynamic impact on endothelial cells (ECs) in AVFs.

Methods: A tubular bifurcation AVF model was constructed, and the disturbed flow was induced near the bifurcation by pulsatile flow. Hemodynamics was simulated using computational fluid dynamics (CFD) and visualized as 2D contour plots. Human Umbilical Vein Endothelial Cells (HUVECs) were cultured on a tailored polycarbonate membrane (PCM) and placed in the model. HUVECs on the PCM allowed precise mapping to the hemodynamic plots.

Results: CFD identified four regions: the outer wall with high time-averaged wall shear stress (TAWSS MAX) and transverse wall shear stress (TransWSS MAX), the inner wall with low and oscillatory wall shear stress (L/O), and the pulsatile flow (PF). HUVECs in PF were aligned in the direction of flow. The cells in other regions showed more focal adhesion junctions and fewer glycocalyces. HUVECs on inner wall had the lowest expression of Krüppel-like factor 2 and endothelial nitric oxide synthase, while the outer wall showed the highest expression of platelet-derived growth factor and transforming growth factor-β.

Conclusions: We developed an *in vitro* AVF model and validated the effects of different hemodynamic profiles on ECs by matching CFD plots with cell positions on a tailored PCM. This study shows that the *in vitro* AVF model can be a promising tool to assess the impact of interventions aimed at improving ECs function in AVFs.

Statement of Significance: **In Vitro Model Development**: An innovative in vitro model was developed to simulate arteriovenous fistula conditions, allowing for direct assessment of endothelial cell behavior under varied hemodynamic conditions. **Linking Hemodynamics to Cell Response**: The research successfully correlated computational fluid dynamics results with specific endothelial cell positions, facilitating a clearer understanding of the impact of hemodynamics on cell morphology and function. **Arteriovenous Fistula Failure Understanding**: The study enhances the understanding of arteriovenous fistula failure mechanisms, specifically the role of intimal hyperplasia caused by disturbed flow.

1. Introduction

An arteriovenous fistula (AVF) is the preferred type of vascular access for hemodialysis in patients with end-stage kidney disease (ESKD). However, approximately 60 % of AVFs require intervention within the first year due to patency issues primarily caused by stenosis

* Corresponding author.
E-mail address: j.i.rotmans@lumc.nl (J.I. Rotmans).

https://doi.org/10.1016/j.actbio.2026.01.044
Received 20 August 2025; Received in revised form 20 January 2026; Accepted 23 January 2026
Available online 24 January 2026

from intimal hyperplasia and insufficient outward remodeling after surgery [1]. Physiological vascular function depends on stable hemodynamics to preserve endothelial cell (EC) morphology and function. After the creation of an arteriovenous anastomosis, the bifurcated vascular configuration and pulsatile flow induce disturbed flow at the anastomotic site, significantly contributing to EC dysfunction and the development of intimal hyperplasia [2]. Various *in vitro* studies have used single-channel chips to explore the effects of disturbed flow, typically characterized by low and oscillatory wall shear stress (WSS), on ECs [3–5]. These studies revealed that disturbed flow promoted EC rounding, misalignment with flow direction and shifting to a pro-inflammatory phenotype by downregulating anti-inflammatory factors and increasing cell permeability through adherens junction remodeling [6–11]. Recently, it has been suggested that the complexities of disturbed flow extend beyond low and oscillatory WSS, with WSS multi-directionality playing a role in EC dysfunction and vascular pathology [12,13]. Thus, solely modeling disturbed flow based on low and oscillatory WSS may underestimate its impact on ECs. Conventional single-channel chips inadequately replicate the complex hemodynamics of disturbed flow due to its simplified geometries [5,14,15]. Previously, we developed a three-dimensional (3D) tubular bifurcation bypass model that effectively induced complex disturbed flow, defined as direction and WSS that varies in space and time [16]. ECs in this model performed heterogeneously under disturbed flow and other hemodynamics conditions. However, accurately mapping local hemodynamic features to cellular responses within 3D structures was not included in this model.

In the absence of direct measurement capabilities for hemodynamic effects on the vascular wall *in vivo*, computational fluid dynamics (CFD) have become a powerful tool for simulating flow and analyzing flow-field distributions. 3D vessels were reconstructed after CT/MRI scanning and hemodynamics were simulated in CFD [17,18]. To map the hemodynamics and biological samples, vessels are divided into uniformly sized mesh elements to assign averaged hemodynamic values [19–21]. However, the spatial accuracy of this method cannot be assured in AVFs. The diameter of a matured AVF is around 6-10mm, and regions affected by disturbed flow near the anastomoses are small. Notably, acquiring intact human vessel specimens for pathological analysis presents a challenge; Even if samples can be obtained, vessel collapse post-excision hinders precise alignment of simulated hemodynamics with histological samples. Addressing these challenges requires a method for high-resolution spatial registration of hemodynamic features with cellular positions, essential for understanding flow-mediated endothelial pathophysiology.

To overcome these limitations, we modified our 3D tubular bifurcation bypass model to an AVF model and enhanced it by integrating a customizable polycarbonate membrane (PCM) acting as a carrier for cell seeding. In the previous bypass model, the flow inlet was located at the bifurcation, making it more representative of an arteriovenous graft model. In contrast, the AVF model relocates the inlet from the bifurcation to the horizontal channel, with the disturbed flow-affected region situated at the bifurcation. This configuration mimics the area prone to IH in the juxta-anastomotic section. The PCM allowed direct exposure of cells to disturbed flow near the anastomotic section and extraction from the model after experiment. By imaging and coordinating processing of PCM, we address the challenge of mapping local hemodynamics features to cellular behavior with sub-millimeter precision in 3D AVF models. The protocol described in this study establishes a robust platform for investigating complex bifurcation hemodynamics and identifying hemodynamic predictors of vascular pathology.

2. Protocol

This protocol consists of three parts. The first and second parts focus on the preparatory work before the flow experiments. The first part details the design of the AVF model and cell seeding, while the second part describes the CFD simulations of the model and the hemodynamic mapping with PCM. The third part utilizes the methods introduced in the first two sections to conduct three cell experiments aimed at verifying the effects of the disturbed flow induced by the model on cell morphology, glycocalyx, and functional markers, Fig. 1A.

Part 1

2.1. Design of the in vitro AVF model and PCM

The *in vitro* AVF model was composed of three core components: an adaptor, a cover plate, and a base plate, along with accessories including silicone waterproof seals and a threaded luer connector. These components were designed in SolidWorks 2020 (Dassault Systèmes, Paris, France) and assembled as illustrated in Fig. 1B-E. The cover plate utilized the same component from our previous bypass flow model, fabricated from polystyrene through plastic injection molding (Arburg 320 KS 700-250, NL). To make the AVF model applicable to the PCM [19], we rebuilt the adaptor and base plate by computer numerical control machine tools (Haas Mini Mill, USA). The adaptor was a transparent poly-methyl methacrylate (PMMA) component with a tubular channel (l3 = 20mm, diameter = 2.5mm) inside, Fig. 1C, H. The adapter was equipped with threads on the top to link the threaded luer connector and the tube of pump, and it also helped fix PCM by compressing to prevent the displacement when the PCM was exposed to flow, Fig. 1C. The lower part of the adapter was a plug designed to fit the socket on top of the cover plate, Fig. 1F. When the cover plate and base plate were assembled, a channel (l = 70 mm, diameter = 2.5 mm) between the two plates was formed (Fig. 1D, E) and channels in the plates and adapter became a 60° bifurcated system after inserting the adaptor into the cover plate, Fig. 1H. To simulate the flow conditions of an AVF, we linked one of the luer connectors to an Ibidi pump system (Ibidi GmbH, Martinsried, Germany) providing an inlet flow. The luer connector on the adapter worked as an outlet, and the last luer connector was blocked by a syringe, Fig. 1I. A piece of 10 μm thick transparent polycarbonate membrane (it4ip, Belgium) was employed as a cell carrier in the adaptor channel of the AVF model. To ensure compatibility with the channel configuration in the adaptor, we projected the channel wall of the adaptor as a 2D blueprint in SolidWorks 2020, which served as a template for PCM tailoring.

2.2. Modification of the Ibidi pump system for enhancing fluid dynamics

The Ibidi system is a liquid pump system that relies on pressure control to generate a pulsatile flow pattern by periodically occluding the enclosed tube by a switch within the system. However, during the occlusion phase, the flow velocity within the tube drops to zero which does not accurately reflect physiological conditions, where blood flow continues at a low velocity during the diastolic phase of the cardiac cycle. To address this limitation, we implemented a simple modification to the Ibidi system. A side tube connected by a 0.6 mm diameter needle at the distal end was added upstream of the main tube. The needle incorporated an in-line luer injection port (Ibidi GmbH, Martinsried, Germany) that allowed for the reflow of fluid back into the main tube, as depicted in Fig. 1I, Experimental design of the AVF model with modification of the Ibidi system. I. When the switch was on, the fluid went through both tubes providing a higher flow velocity. When the switch was off, the main tube was compressed and the flow velocity declined significantly due to the small diameter of the needle. By adjusting the air pressure of the pump to 75 millibar, we induced a pulsatile flow rate of 3–18 mL/min (Frequency = 1 Hz). Each cycle consisted of a high flow rate phase of 6.11 cm/s (18 mL/min) for 0.5 seconds and a low flow rate phase of 1.02 cm/s (3 mL/min) for the remaining 0.5 seconds, Fig. 1J, Experimental design of the AVF model with modification of the Ibidi system. J. The flow rates were calibrated by measuring the volume of liquid collected in a syringe over one minute following the operational guidelines from manufacturer. The perfusion fluid used in the Ibidi

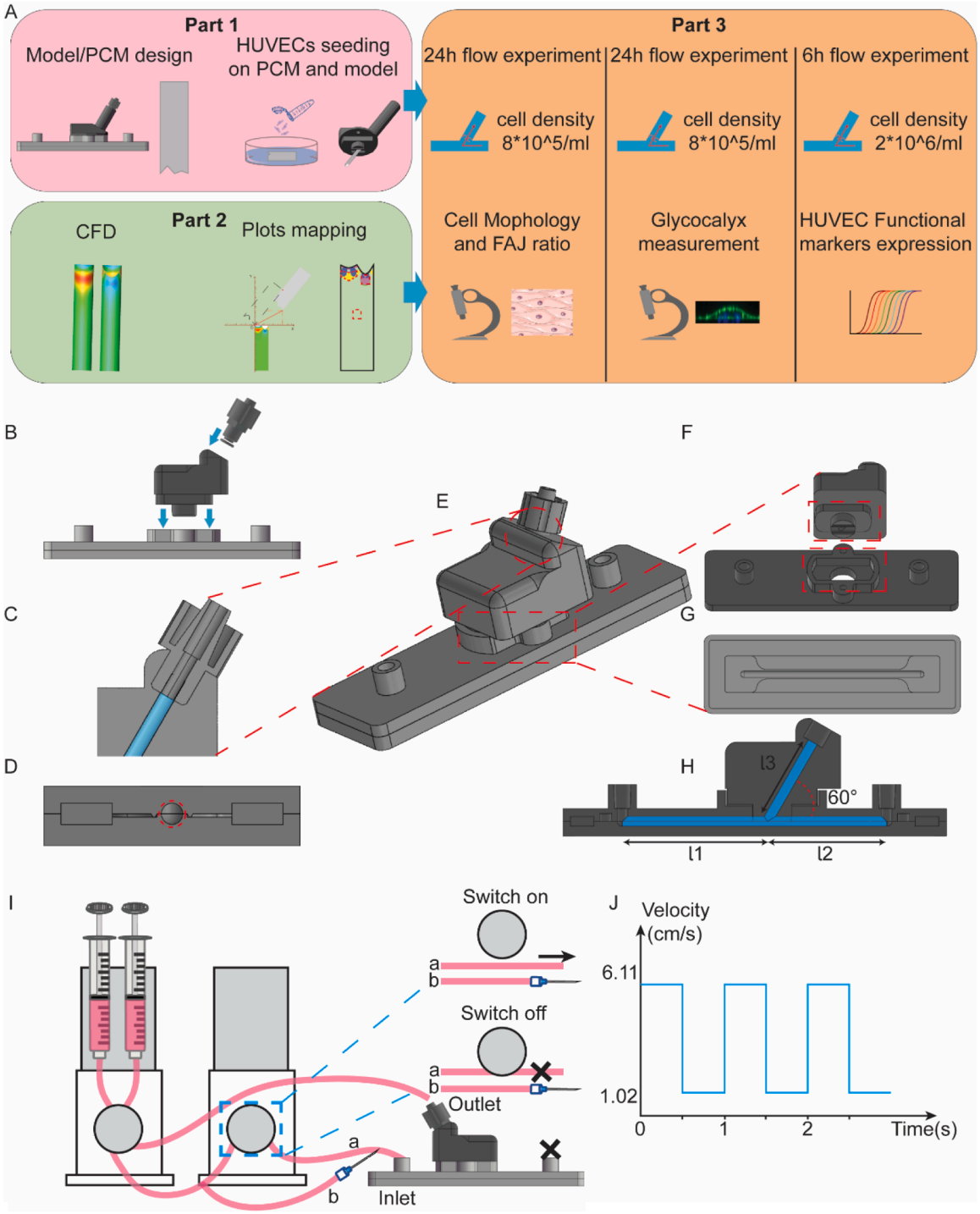

Fig. 1. Experimental design of the AVF model with modification of the Ibidi system. A, the flow chart of this study; B-H, design of the AVF disturbed flow model. B, the disassembled model include adaptor, cover plate, base plate and Luer connector. C, Luer connector fixes the PCM (light blue color) after inserting it into the adaptor. D, cross-sectional view of the assembled cover and plate, the diameter of the channel is 2.5 mm (red circle). E, overview of the assembled model. F, the bottom view of the adapter shows the plug in the red rectangle, top view of the cover plate shows the socket in the red rectangle. G, top view of the plate shows the semi round channel. H, longitudinal section view of the model shows the 60°bifurcated tubular channel inside the model (deep blue), l1 = 39.45 mm, l2 = 30.55 mm, l3 = 20 mm; I-J, the modification of Ibidi pump system. I, overview of the tube connection in the system. Both the main tube (a) and side tube (b) are open when the switch is off. Only the side tube is open when the switch is on. J, waveform of the flow based on the modification of the pump system, frequency = 1 Hz, max velocity = 6.11 cm/s, min velocity = 1.02 cm/s.

pump system consisted of complete endothelial cell culture medium (EGM-2, PromoCell) supplemented with 0.7 mg/mL xanthan gum (Sigma-Aldrich) to mimic blood viscosity [22,23], with the culture medium being refreshed daily.

2.3. Seed HUVECs on PCM and load into the AVF model

Primary Human Umbilical Vein Endothelial Cells (HUVECs; Leiden University Medical Center, The Netherlands) were isolated from umbilical cords provided by the Department of Obstetrics at Leiden

University Medical Center, following the methodology described before [24]. Cells were cultured in complete endothelial cell growth medium 2 (EGM-2, PromoCell), supplemented with 50 U/mL penicillin/streptomycin (Gibco) and Supplement Mix (PromoCell). The cells were cultured on plates pre-coated with 1 % gelatin (Merck) solution in PBS until the 3rd to 4th passage. Once reaching 80 % confluency HUVECs were re-suspended to a concentration of 0.8×10^6/mL or 2×10^6/mL for further use.

A piece of 10 μm thick PCM was tailored into a rectangular section measuring 20 mm x 7.81 mm. One end shaped like the 2D blueprint of tube wall to fit the anastomotic section. Both sides of the PCM were disinfected for 30 min each by ultraviolet light and penicillin/streptomycin. Then, a filtered solution of 2 mg/mL (w/v) poly(dopamine) (PDA) (Merck, cat. no. H8502-5G) was dissolved in 10 mM Tris·Cl buffer (pH 8.5) for crosslinking with the PCM [25,26]. After 2 h crosslinking, excess PDA was washed away by PBS, following coating with a 0.1 % solution of Cultrex 3-D Culture Matrix Rat Collagen I (R&D Systems) for 1 h. HUVECs suspension was dropped onto the coated PCM and cultured in a 37°C incubator with 5 % CO2 in a static condition for 24 h, Fig. 2A. The following day, the cell-seeded PCM was carefully rolled and inserted into the adapter channel lumen from the plug side with fine tweezers, ensuring proper contact of the PCM with the shape of anastomosis section and fixature by Luer connector from the top side, Fig. 2B, D, E, F. Finally, the cover plate, base plate and adaptor were assembled as an AVF model and connected to the Ibidi pump, Fig. 2G. We compared this seeding procedure with our previous method in which cells were seeded after model assembly, supplementary method and Fig. 2H. Within the current cell seeding strategy, the cell layer formed a uniform distribution on both inner and outer walls, after a one-day flow exposure, Fig. 2I. In contrast, on the PCM which seeded the cell after assembling, cells primarily aggregated on the inner wall due to gravity, resulting in uneven distribution on the outer wall, Fig. 2H.

Part 2

2.4. Computational fluid dynamics conditions

CFD was used to validate the flow and predict the hemodynamics in the AVF model channel. Preprocessing was conducted using the ANSYS ICEM CFD 2022 R1 software (ANSYS Inc., Pittsburgh, PA, USA) to create structural meshes with the detailed mesh representation depicted in Fig. 3A, C. Subsequently, comprehensive mesh and timestep independent studies were executed to guarantee the stability of computational outcomes, Table S1, S2. The solution was considered mesh-independent or timestep-independent when the change in this value was below 1 % upon further refinement. The final mesh consisted of approximately 3,200,107 elements, including 15 boundary layers, and exhibited high quality (minimal orthogonality quality = 0.41).

The fluid was modeled as a uniform, isothermal, incompressible Newtonian medium with a density (ρ) of 1020 kg/m^3 and a dynamic viscosity (μ) of 3.5 cP. The peak Reynolds number Re = ρUD/μ, where U is the peak velocity (0.0611 m/s) and D is the diameter (0.0025 m), was approximately 45, confirming that the flow was laminar throughout the cardiac cycle. The governing equations were Navier-Stokes equation and Continuity equation:

$$\rho\frac{\partial\vec{u}}{\partial t}+\rho(\vec{u}\cdot\nabla)\vec{u}+\nabla p-\mu\nabla^2\vec{u}=0 \quad (1)$$

$$\nabla\cdot\vec{u}=0 \quad (2)$$

where $\vec{u}$ is the flow velocity vector, p is the pressure, ρ is the medium density of 1020 kg/m^3 [27], μ is the dynamic viscosity 3.5 cP [28]. A fully developed pulsatile flow profile was applied at the inlet. The inlet flow was applied as a square-wave pulse, Fig. 1J, Experimental design of the AVF model with modification of the Ibidi system. J, following the pattern provided by the Ibidi system. The peak and minimum flow velocities were 6.11 cm/s and 1.02 cm/s, respectively. At the outlet, A standard outflow boundary condition was applied, which imposes a Dirichlet condition of zero pressure (p = 0), combined with a zero normal gradient for the velocity field ($\partial\mathbf{u}/\partial n = 0$).

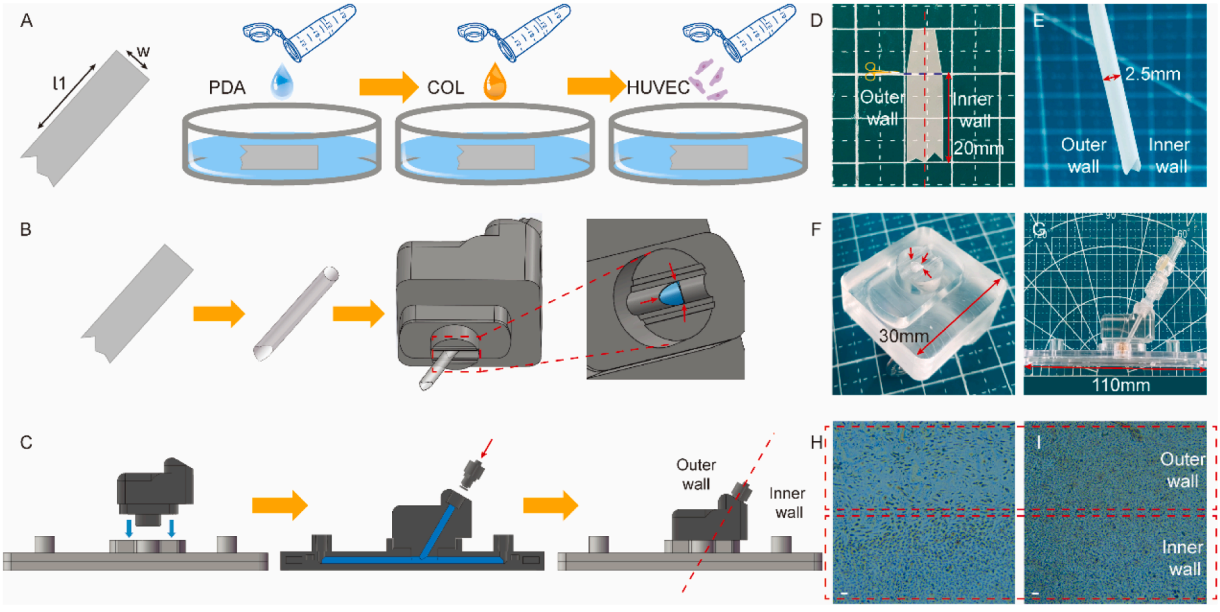

Fig. 2. PCM works as a HUVECs carrier in the AVF model. A, the tailored PCM is crosslinked with PDA, coated with collagen and seeded with HUVECs, l1 = 20mm, w = 7.81mm. B, the PCM is rotated and inserted into the bifurcation of AVF model, the light blue represents the PCM when covering the bifurcation wall, the red arrows show the proper coverage of the PCM with the anastomosis section. C, AVF model is assembled with separate parts. D, the translucent PCM sample shows the boundary of inner and outer walls (red dash line). The part of the PCM above the black dash line is used for tweezer clamping and removed after insertion. E, the rotated PCM as a tube. F, the adaptor inserted with PCM, the red arrows show the proper coverage of the PCM with the anastomosis section. G. the overview of the assembled AVF model. The PCM in the bifurcation can be seen through the transparent PMMA adaptor. H-I, the overview of HUVECs distribution on the PCM after seeding after PCM insertion (H) or before PCM insertion (I), scale bar = 100μm.

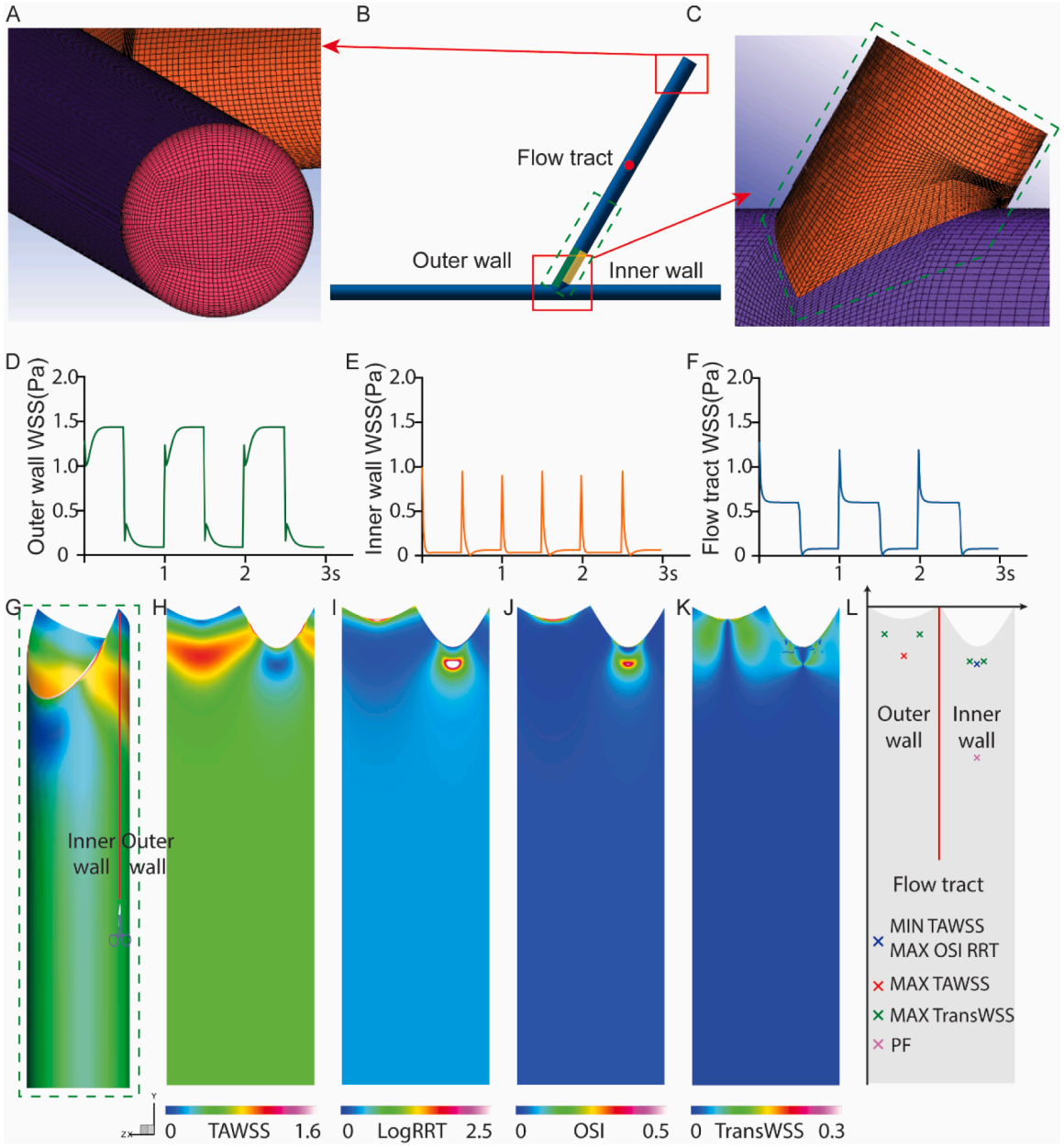

Fig. 3. Hemodynamics in the channel of AVF model. A, the plot of structural meshes in the outlet. B, the fluid domain in the AVF model, the green dash area is the bifurcation part of the AVF model, the red dots show the location of the flow tract, the yellow and green regions show the inner wall, and outer wall of the bifurcation. C, the plot of structural meshes around the anastomosis section. D-F, the variation of temporal WSS on the outer wall, inner wall and flow tract. G, the contour plot of the TAWSS on the 3D AVF bifurcation, the red line is the boundary of outer and inner walls. H-K, 2D contour plot of TAWSS, TransWSS, RRT, OSI. L, the coordinate system for 2D contour plot in Tecplot 360 and the location of specific hemodynamics point, the left upper vertex of the plot is merged with the origin, the contour plot is in the second quadrant.

The equations were solved using a finite volume method in ANSYS Fluent 2022 R1, employing a fully implicit, second-order backward Euler differencing scheme. The convergence criterion was set to 10^{-8} based on normalized residuals. Following the time-step independence study, a time-step size of 0.01 s was chosen. To avoid startup transients, simulations were run for three cardiac cycles, and results from the third cycle were used for analysis.

The formulas of time-averaged WSS (TAWSS), oscillatory shear index (OSI), relative residence time (RRT) and transverse WSS (TransWSS) are shown as follows:

$$\mathrm{TAWSS} = \frac{1}{\mathrm{T}} \int_0^{\mathrm{T}} |\vec{\tau_w}| \mathrm{dt} \tag{3}$$

$$\mathrm{OSI} = 0.5 \left[1 - \frac{\left| \int_0^{\mathrm{T}} \vec{\tau_w} \mathrm{dt} \right|}{\int_0^{\mathrm{T}} |\vec{\tau_w}| \mathrm{dt}} \right] \tag{4}$$

$$\mathrm{RRT} = \frac{1}{(1 - 2 \cdot \mathrm{OSI}) \cdot \mathrm{TAWSS}} \tag{5}$$

$$\mathrm{TransWSS} = \frac{1}{T} \int_0^T \left| \vec{\tau_w} \cdot \left(n \times \frac{\int_0^T \vec{\tau_w} dt}{\left| \int_0^T \vec{\tau_w} dt \right|} \right) \right| \tag{6}$$

Where T is a cardiac cycle of pulsation and $|\vec{\tau_w}|$ is an instantaneous wall shear stress vector, n is the normal vector to the surface.

Post-processing was performed in MATLAB 2020 (MathWorks, USA)

and final visualizations were generated using Tecplot 360 EX 2020 RI (Tecplot, Inc, USA).

2.5. Computational fluid dynamics simulate the hemodynamics in the AVF model

We recorded the transient wall shear stress (WSS) from the location with the highest value on the outer wall or the lowest value on the inner wall, Fig. 3B. The WSS on the flow tract wall 10mm away from the anastomosis section was also recorded. The periodic variation of WSS plot confirmed that the modified Ibidi system induced a continuous pulsatile WSS waveform in the AVF model. During the high-flow phase, the outer wall exhibited a higher WSS (1.44 Pa) compared to the inner wall (0.07 Pa) and the flow tract (0.70 Pa). While during the low-flow phase, the WSS on the outer wall was slightly higher compared to the other two locations (outer wall, 0.09 Pa; inner wall, 0.04 Pa; flow tract, 0.08 Pa). The variability in WSS on the outer wall was notably greater than that of the inner wall, which remained at extremely low levels throughout the cycle, except for brief spikes attributed to fluctuations when Ibidi system's valve was toggled to induce pulsatility every 0.5s, Fig. 3D-F. Notably, a transient spike in WSS was observed on the inner wall immediately following the step increase or decrease in inlet flow. This is likely due to the rapid acceleration or deceleration of the bulk flow, which can induce transient flow reversal and the strengthening of secondary flow vortices in this region, momentarily increasing the local velocity gradient at the wall. This complex response highlights the spatiotemporal complexity of disturbed flow, where WSS is not a simple function of the bulk flow rate.

As the original CFD plot was a 3D tubular configuration which was challenging to map the PCM, we transformed the 3D tube into a 2D contour plot along the boundary between the inner and outer wall based on the method described in the manual of Tecplot 360, Fig. 3G, L. The 2D contour plot revealed that the most significant hemodynamic alterations occurred within 3 mm of the anastomotic site. Notably, regions of peak and minimum values were localized in proximity to each other, Fig. 3H-K. Afterwards, a coordinate system was established with the upper-left point at the anastomosis as the origin. Given that the outer wall is characterized by high WSS, we pinpointed the coordinates for the maximum TAWSS (TAWSS MAX) of the entire contour plot, where OSI, RRT, and TransWSS remained low. The maximum TransWSS (TransWSS MAX) was positioned 1.48 mm superior and to the left of TAWSS MAX, Fig. 3L, Table 1. In contrast, the inner wall was characterized by low and oscillatory hemodynamics. The coordinates of the lowest TAWSS and highest OSI/RRT coincided at the same location on the inner wall. Notably, we also identified a maximum TransWSS point on the inner wall, which was slightly lower than that on outer wall, and it was only 0.2 mm from the lowest TAWSS and highest OSI/RRT point, Fig. 3L, Table 1. The hemodynamics at the distal end of the flow tract were more stable than near the anastomosis. A point on the inner wall located 10 mm from the anastomosis was selected as the pulsatile flow (PF) region, characterized by TAWSS = 0.44 Pa, OSI = 0.02, logRRT = 0.38, and TransWSS = 0 Pa, Fig. 3L, Table 1.

2.6. Immunofluorescent staining

After the flow experiment, the model was disassembled, and the PCM was extracted from the adaptor channel, ensuring the cell layer on the PCM faced upwards. The PCM was then fixed in 4 % paraformaldehyde for 10 min, and cells were permeabilized by incubating with 0.3 % Triton-X100 in PBS for 10 min, following incubation with 5 % bovine serum albumin (BSA, Sigma-Aldrich) in PBS for 30 min.

For cell morphology staining, the samples were incubated overnight at 4°C with the primary VE-cadherin antibody (purified Mouse Anti-Human CD144, BD, 1:200). After washing the samples three times with PBS, samples were incubated at room temperature for 1 h with appropriate secondary antibody (Alexa Fluor 647 goat anti-mouse IgG, Invitrogen) in presence of phalloidin-Rhodamine (Invitrogen) and Hoechst (Molecular Probes) in 0.5 % BSA/PBS solution. For the study of glycocalyx staining, the samples were incubated for 1 h with FITC labeled wheat germ agglutinin (FITC-WGA, Sigma Aldrich, 1:400) and Hoechst (Molecular Probes) in 0.5 % BSA/PBS solution.

Images were captured using a Dragonfly-200 confocal microscope (Andor Technology, Belfast, UK) equipped with a 63x (NA 1.52) or 40x (NA 1.33) objective. During GLX imaging, a z-stack scanning approach was employed to capture images of the endothelial cells in successive layers.

2.7. Match PCM co-ordinate from confocal microscope system with 2D contour plot

Due to the elasticity and stiffness of the PCM, the immunofluorescence-stained samples were flattened on glass cover slides and imaged under 40x (NA 1.33) objective of the confocal microscope, Fig. 4A. The montage mode was utilized to stitch the images and group as a comprehensive image of the entire PCM. The comprehensive image showed that the HUVEC layer was intact across the PCM, with a small number of cells detached from the anastomosis regions, Fig. 4B.

To match the comprehensive image of the PCM and the CFD plot *in silico*, we first aligned the center of the viewing field with the upper and lower vertices (**a, b**) on the left edge of the PCM, recording their coordinates in the Confocal Laser Scanning Microscope (CLSM) system, **a** (x1, y1), **b** (x2, y2), Fig. 4C. After merging the CLSM and CFD coordinates system, we translated PCM and overlapped the vertex **a** with the origin by the Axis Formula, Supplementary Equation 1. The new coordinates of a (0, 0), b (x2-x1, y2-y1) and the new position of PCM in the merged coordinates system were shown in Fig. 4D. Subsequently, the PCM was rotated θ degrees to the second quadrant of the CLSM coordinates system by the Rotation Matrix Formula, Supplementary Equation 2 and Fig. 4E. After the two-step transformation, the six coordinates of TAWSS MAX/ TransWSS MAX/RRT MAX/OSI MAX, TAWSS MIN, PF on the PCM were in the same position as the CFD plot, Fig. 4F. Through reverse calculation, the original coordinates of the six points in the CLSM coordinate system were derived, immunofluorescence images of these points could be easily targeted by adjusting the confocal microscope controller, Supplementary Coordinates calculator. Additionally, we segmented the PCM into outer wall and inner wall regions based on the center line of the PCM and the relative position of PCM in the

Table 1
Hemodynamics characteristics, coordinates in various locations on outer and inner wall of the AVF model bifurcation.

	Location	TAWSS [Pa]	OSI	logRRT [1/Pa]	TransWSS [Pa]	X [mm]	Y [mm]	Distance [mm]	
Outer wall	TAWSS MAX	1.04	0.00	-0.02	0.01	1.87	-2.57	reference	-
	TransWSS MAX	0.67	0.01	0.18	0.09	2.85	-1.46	1.48	-
Inner wall	TAWSS MIN	0.09	0.48	2.41	0.00	5.84	-3.05	-	reference
	TransWSS MAX	0.11	0.30	1.35	0.08	5.66	-2.97	-	0.20
	OSI MAX	0.09	0.48	2.41	0.00	5.84	-3.05	-	0.00
	RRT MAX	0.09	0.48	2.41	0.00	5.84	-3.05	-	0.00
	PF	0.44	0.02	0.38	0.00	5.90	-10.00	-	6.95

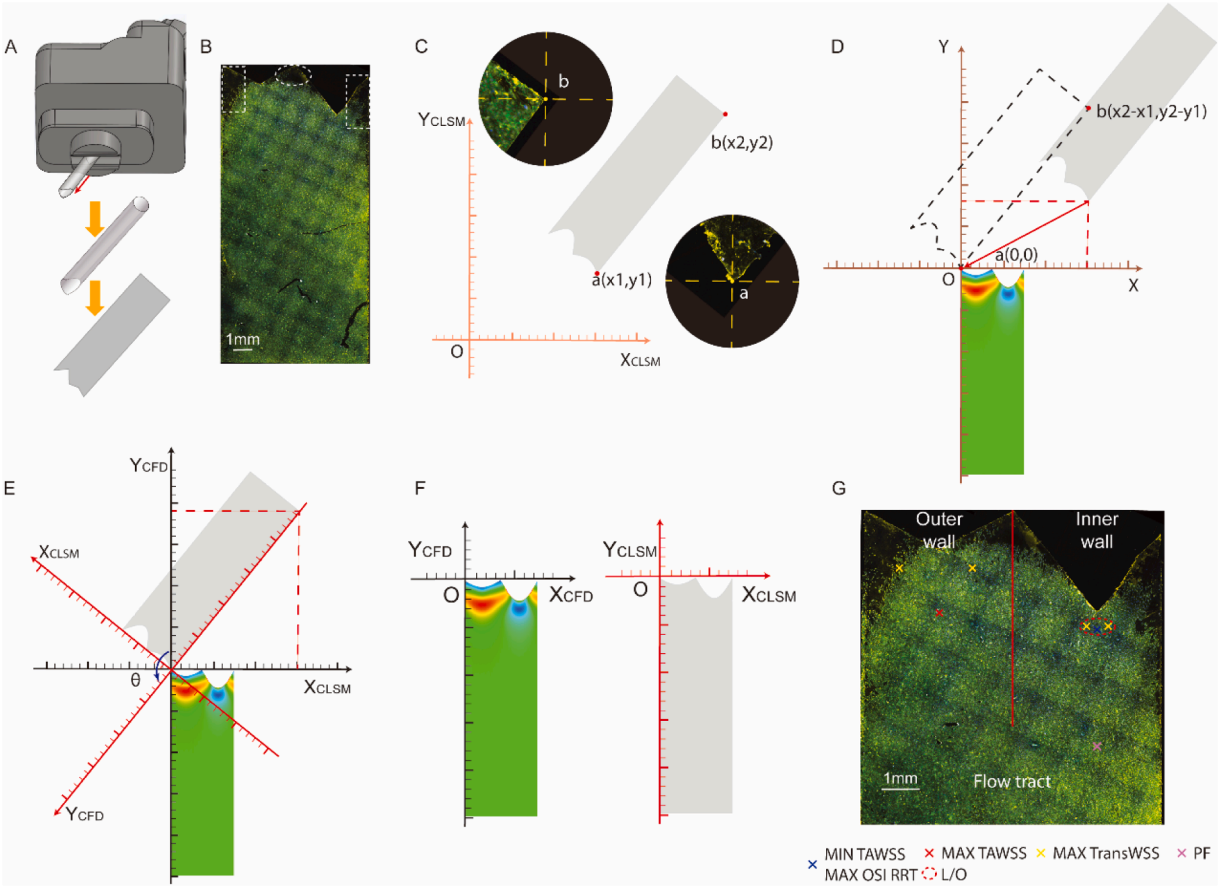

Fig. 4. Map of PCM coordinates in confocal microscope with hemodynamics property in CFD co-ordinates. A, the rotated PCM from the tube in the adapter and flattened on a glass cover slide. B, the overview of the fluorescence image of HUVECs on the flattened PCM. The white dash areas show the detached regions of the HUVECs, scale bar = 1mm. C, the coordinate system of the PCM in the confocal microscope system (X_{CLSM}, Y_{CLSM}). a (x1, y1) and b (x2, y2) are the upper and lower vertices on the left edge of the PCM. Coordinates of a and b are extracted from the confocal microscope system. D, a (x1, y1) translated to the origin by the Axis Formula. E-F, rotated θ degrees by the Matrix Rotation formula to merge the coordinates of PCM to the co-ordinates of 2D contour plot. G, map the coordinates of MIN TAWSS, MAX OSI, MAX RRT, TAWSS MAX, TransWSS MAX and PF from the CFD 2D contour plot with the cells on PCM, the red dash circle is the L/O area, scale bar = 1mm.

adapter channel. However, due to the proximity of the TransWSS MAX/RRT MAX/OSI MAX, TAWSS MIN on the inner wall, the images were overlapped within these positions, therefore, we categorized them as low and oscillatory points (L/O) based on their hemodynamic characteristics, Fig. 4G. Notably, since there were two distinct TransWSS MAX regions on the outer wall, the point close to the PCM edge was eliminated to minimize the influence of cell detachment in this region. Finally, four points TAWSS MAX, TransWSS MAX, L/O and PF were selected for the subsequent analysis in this study.

Part 3

2.8. Cell morphology and cell junction analysis

The HUVECs (cell density 0.8×10^6/mL) in the model were exposed to the pulsatile flow provided by the IBIDI system for 24 h to study the changes in cell morphology. Cell morphological features and adherens junction lengths were extracted from confocal microscopy images using ImageJ. Cell borders were identified based on VE-cadherin staining. Cell alignment was defined as the absolute angle between the cell major axis and flow direction, while elongation was assessed using the major/minor axis ratio and eccentricity [29]. Morphological distributions were visualized via violin plots with median and interquartile range (IQR). Adherens junctions were classified into stable adherens junctions (AJs) characterized as parallel F-actin alignment with VE-cadherin, while focal adherens junctions (FAJs) were connected to F-actin bundles and aligned perpendicularly to VE-cadherin [30]. Spatial colocalization of VE-cadherin and F-actin was validated in ImageJ-win64 (Fiji) [31]. The ratio of FAJ length over total junction length (AJs + FAJs) was calculated to quantify junctional remodeling. For each region of interest, 25 cells were analyzed.

2.9. Glycocalyx coverage quantification

The HUVECSs within the model were subjected to the pulsatile flow for a duration of 24 h to investigate the alterations in Glycocalyx. Glycocalyx coverage was evaluated in both xy-plane and z-direction. For the xy-plane analysis, maximum intensity projections of all *z*-stack images were performed, and the mean fluorescence intensity (Mean FL) across the field of view was calculated in imageJ [32]. To quantify the glycocalyx coverage in *z*-direction, resliced images from a line (10 pixels wide) over the nucleus were drawn at the nuclear position. Fluorescence intensity was calculated based on the mean FL from the half-maximum signal of the nuclear staining to the half-maximum signal at the luminal end of the staining in the *z*-direction. The thickness of the glycocalyx was quantified by calculating the distance from the half-maximum signal of the nuclear staining to the half maximum signal at the luminal end of the staining in the *z*-direction. Surface amounts of glycocalyx were presented as mean FL multiplied by thickness [33,34].

2.10. Quantitative reverse transcription-polymerase chain reaction (qPCR)

The HUVECs (cell density 2.0 × 10^6/mL) in the model were exposed to the pulsatile flow for 6 h to study the changes of functional markers level. The PCM with cells was cut into 1.5mm by 1.5mm samples based on the hemodynamic conditions. Total RNAs were extracted by RNeasy Mini Kit (Qiagen). RNA was reverse-transcribed into cDNA by a M-MLV Reverse Transcriptase Kit (Promega, Singapore). Afterwards, qPCR was performed with SYBR Select Master Mix (Waltham, MA, USA; Applied Biosystems) in Bio-Rad CFX384 Touch™ Real-Time PCR Detection System. Primers were designed based on the NCBI reference sequence database, Supplementary Table 3.

2.11. Statistical analysis

All data shown in violin graphs were presented as median (plus interquartile range, IQR). The data shown in bar graphs were presented as means ± SEM, while n representing the number of biological independent experiments. Groups were compared by one-way ANOVA, and $P < 0.05$ was considered statistically significant. If a significant difference was detected, post-hoc comparisons were performed using Tukey's multiple comparisons test to identify the specific groups that differed.

3. Results

3.1. Cell morphology variation and FAJ ratios across hemodynamic regions

The cells exhibited distinct morphologies among the four hemodynamic feature regions. We collected a total of 817 cells from TAWSS MAX (n = 205), TransWSS MAX (n = 192), L/O (n = 233), and PF (n = 187), Fig. 5A.

Cell alignment was defined as the orientation between the major axis of the cell and the direction of flow. The violin plots revealed that cells in the PF were highly aligned with the flow direction, exhibiting a median alignment angle of 14.42° (IQR, 6.78°, 27.24°). In contrast, cells at the TAWSS MAX (35.80°, IQR, 17.25°, 64.89°) and L/O (48.44°, IQR, 31.75°, 69.65°) showed no significant alignment tendency. Interestingly, cells at the TransWSS MAX displayed an orientation perpendicular to the flow direction with a median angle of 67.12° (IQR, 37.35°, 81.62°), Fig. 5B, F.

To quantify cell elongation, we assessed both eccentricity and the ratio of the major to minor axis [41]. The shape of HUVECs in L/O tended to be round, the median eccentricity was 0.66 (IQR, 0.54, 0.76), and the median ratio was 1.46 (IQR, 1.26, 1.79). While PF showed the greatest elongation, with a median eccentricity of 0.84 (IQR, 0.71, 0.90) and a median ratio of 1.86 (IQR, 1.42, 2.3). The cell morphology at TAWSS MAX and TransWSS MAX was similar, with TAWSS MAX showing a median eccentricity of 0.73 (IQR, 0.60, 0.80) and a median ratio of 1.66 (IQR, 1.34, 2.03). For the TransWSS MAX, the median

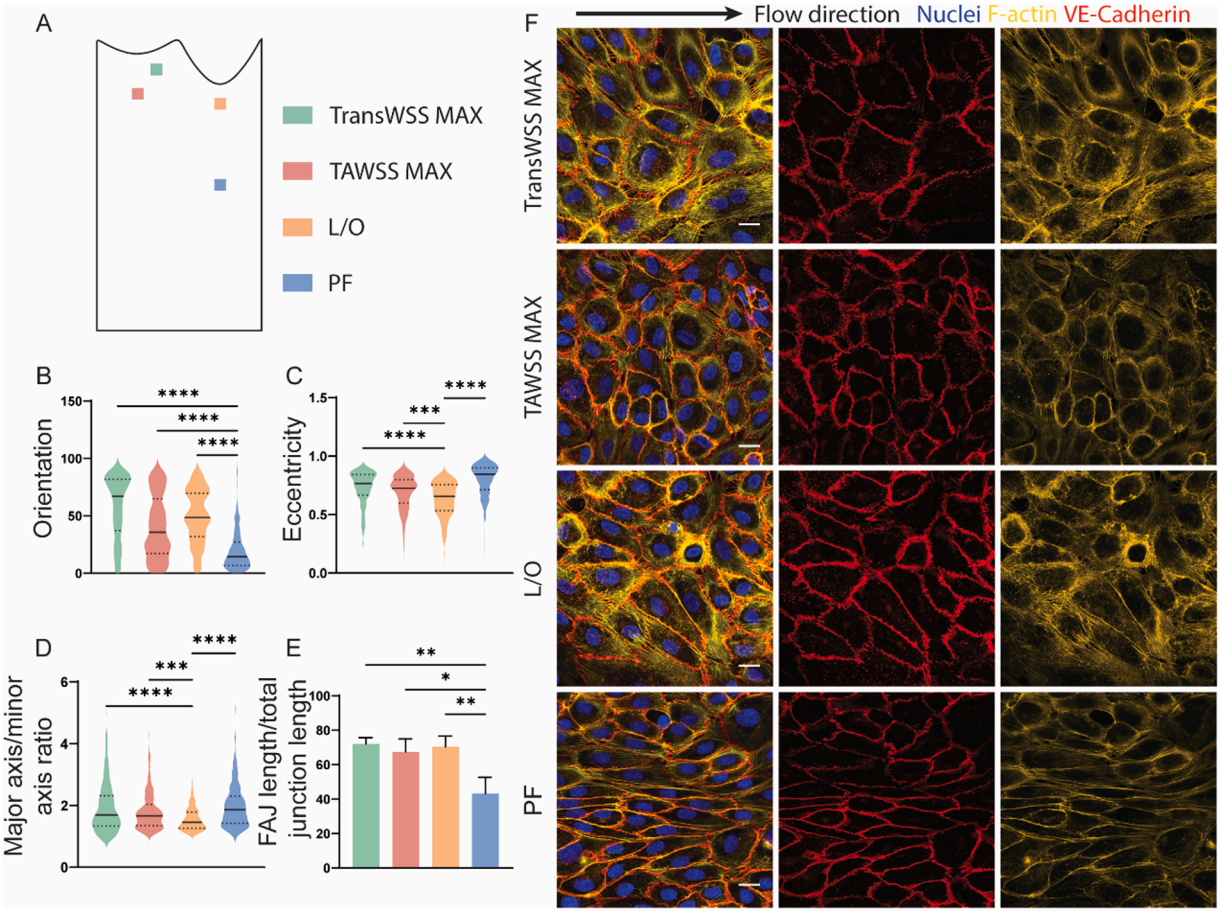

Fig. 5. Cell morphology of HUVECs under different flow conditions. A, the locations of TransWSS MAX, TAWSS MAX, L/O and PF on the PCM. B-D, Violin graphs show the distribution of HUVECs orientation, eccentricity, ratio of major axis/minor axis in TransWSS MAX, TAWSS MAX, L/O and PF. E, Ratio of FAJs length over total adherens junction length in TransWSS MAX, TAWSS MAX, and L/O compared with PF. F, fluorescence images of HUVECs in TransWSS MAX, TAWSS MAX, L/O and PF, scale bar = 20μm. n = 3.

eccentricity was 0.75 (IQR, 0.66, 0.84) and the median ratio was 1.69 (IQR, 1.33, 2.32). No significant differences were observed between these two groups, Fig. 5C-F.

One day after the initiation of flow, the adherens junctions of HUVECs at the TransWSS MAX, TAWSS MAX, and L/O regions exhibited a higher degree of remodeling compared to the PF region, Fig. 5E, F. The adherens junctions on both sides of the channel showed typical characteristics of focal adherens junctions (FAJs) even if the hemodynamics conditions were opposite. The FAJs were aligned perpendicularly to the adherence junctions, with spatial overlaps of VE-cadherin and F-actin within the FAJs. Fluorescence imaging revealed that the peripheral F-actin in PF was more abundant compared to the regions near anastomosis. In PF, VE-cadherin displayed a linear and continuous signal, whereas in the other three locations, VE-cadherin signals were discontinuous and under stress, Fig. 5F. Quantitative analysis of the ratio of FAJ length to total junction length indicated that the FAJ lengths at TransWSS MAX, TAWSS MAX, and L/O were significantly greater than those observed in the PF region, Fig. 5E.

3.2. Impact of hemodynamics on endothelial cell glycocalyx expression

The different hemodynamic conditions had a significant impact on the expression of glycocalyx coverage on ECs. TAWSS MAX, TransWSS MAX on the outer wall, and the L/O on the inner wall showed a notably lower amount of WGA signal on nuclei surface when compared to that expressed in PF. The amount of nuclei surface WGA demonstrated a gradient decreasing trend across TAWSS MAX, TransWSS MAX and L/O, the resliced images revealed un-uniform layer of glycocalyx covering the nuclei, Fig. 6A-E. The mean fluorescence intensity of PF was higher than that of TAWSS MAX, TransWSS MAX, and L/O, while it did not show any difference between latter three regions, Fig. 6F.

3.3. Assessment of gene expression changes in HUVECs under altered hemodynamics

The effect of altered hemodynamics on HUVECs was evaluated by measuring the expression of various function markers by RT-qPCR. Given that RT-qPCR required a certain number of cells for total RNA extraction, it was attempted to select cells from defined areas (1.5 mm x 1.5 mm) centered around TAWSS MAX, TransWSS MAX, L/O, or PF.

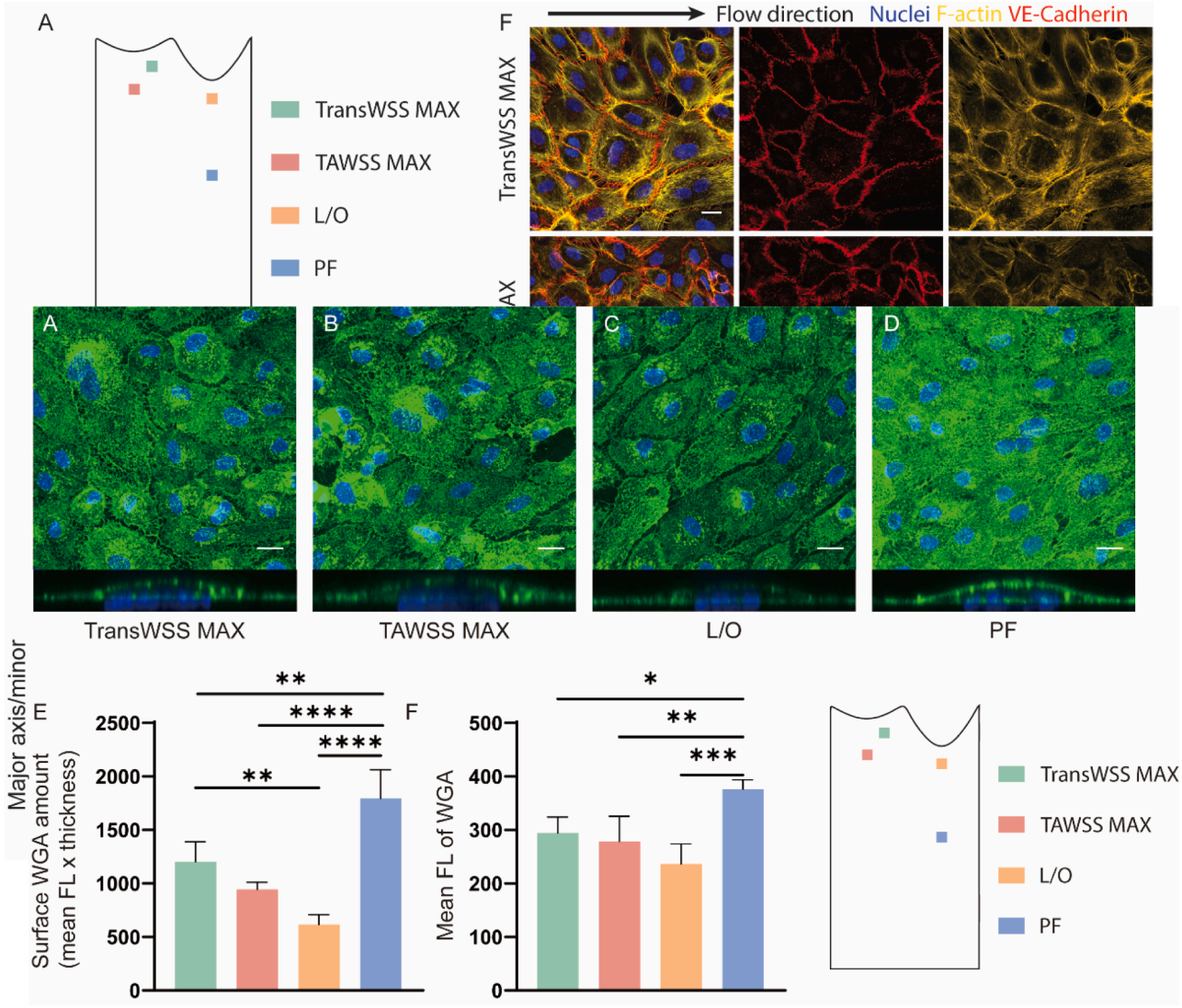

Fig. 6. Glycocalyx of HUVECs under flow different flow conditions. A-D, En face Z-projections and orthogonal views are shown for cells stained for WGA after exposure to TransWSS MAX, TAWSS MAX, L/O and PF, scale bar = 20μm. E, quantification of HUVECs surface WGA expression (mean fluorescence intensity x WAG thickness) in TransWSS MAX, TAWSS MAX, L/O and PF. F, mean fluorescence intensity of WGA from TransWSS MAX, TAWSS MAX, L/O and PF. n = 3.

However, due to the proximity of the points, overlap was inevitable in TAWSS MAX and TransWSS MAX on the outer wall, Fig. 7A. Hence, we selected areas named outer wall, inner wall and flow tract centered around TAWSS MAX, L/O, and PF, respectively, Fig. 7A. Heatmap revealed that outer wall was characterized by high TAWSS and TransWSS, along with low OSI and RRT, while the inner wall exhibited low TAWSS and high OSI, RRT, and TransWSS. The outflow tract demonstrated moderate TAWSS with lower values of OSI, RRT, and TransWSS, Fig. 7B. The RT-qPCR results indicated that, when compared to the outer wall and flow tract, the expression of KLF2 and eNOS was downregulated in the inner wall. Additionally, the expression of PDGF and TGFβ were significantly higher in the outer wall compared to flow tract and inner wall. No significant differences in the expression of ICAM1 and MCP1 were observed across the different regions, Fig. 7C.

In this study, we developed a standardized 60° AVF CFD model to simulate hemodynamic parameters under continuous pulsatile flow which generated by a modified Ibidi system. The 2D contour plotted the spatial distributions of key hemodynamics parameters along the bifurcated channel lumen. Guided by CFD results, a 3D tubular bifurcation system with 60° angulation was fabricated replicating AVF vascular

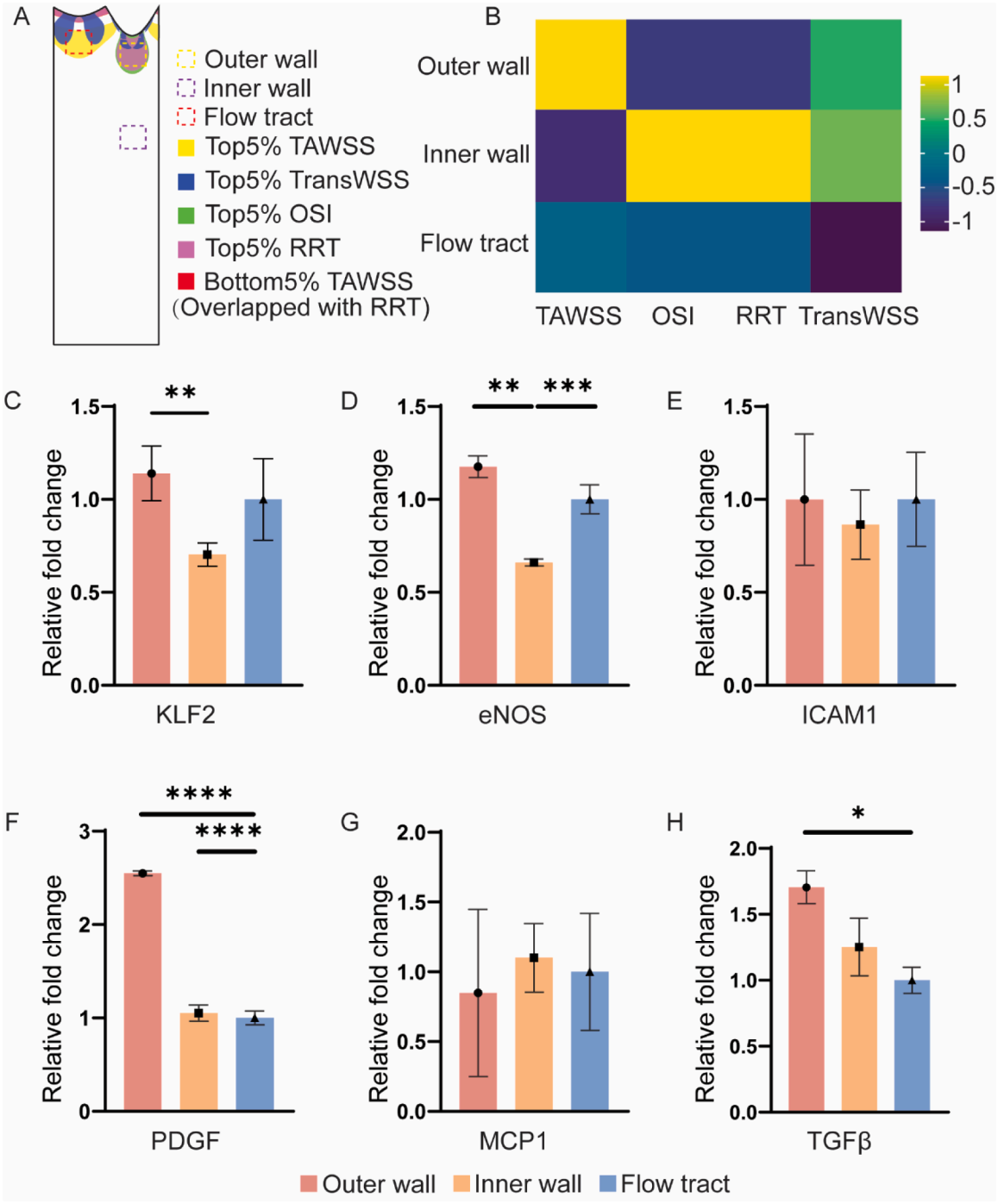

Fig. 7. The relative gene expression of outer wall, inner wall and flow tract. A, the dash rectangle areas showed the locations of the sampled HUVECs from PCM, the 2D contour plots show the distribution of the top 5 % TransWSS, TAWSS, OSI, RRT and the bottom 5 % TAWSS on the PCM. B, heatmap shows the hemodynamics properties of outer wall, inner wall and flow tract, the average hemodynamic values are normalized by z-score. C-H, Comparison of relative gene expression from outer wall, inner wall from flow tract. C, KLF2. D, eNOS. E, ICAM1. F, PDGF. G, MCP1. H, TGFβ. n = 4.

geometry. This system induced a disturbed flow characterized by spatiotemporal variations in velocity and direction at the bifurcation wall within 3mm from the anastomosis section. HUVECs cultured on 10-μm thick PCM, which was inserted into the bifurcation of the AVF model as a cell carrier could be used after flattening to map the coordinates with the 2D hemodynamics contour by mathematical transformation, enabling precise correlation between hemodynamic parameters and cell positions. Notably, HUVECs near the bifurcation exhibited significant structural and functional alterations regardless of outer or inner wall, when compared to the flow tract region. This methodology established a new framework for achieving precise spatial matching between CFD results and cellular experimental outcomes in vascular pathology studies.

The PCM served as an effective cell carrier for the AVF model, enabling simulation of ECs distribution in large tubular vessels. PCM is commonly used as transwell inserts for cell culture with well-documented biocompatibility and low cytotoxicity [35–37]. The polycarbonate material provides sufficient mechanical strength and flexibility for model implantation even with a thickness of only 10 μm. To avoid gravity-induced cell detachment and uneven distribution between outer and inner wall on the channel, HUVECs were seeded on a flat PCM which was crosslinked with PDA and collagen. After 24-hour culturing, the cell-seeded PCM was carefully rolled and inserted into the AVF model with fine forceps for precise alignment with the lumen. Due to the substantial impact of cell density on the morphology, alignment, and formation of FAJ in response to flow, a cell density of 0.8×10^6 cells/cm^2 was selected for studying flow-induced morphological changes. This is consistent with previous literature, which indicates that cells need sufficient space at an appropriate low density to align and elongate along the direction of blood flow [11]. However, a significant number of cells at the edges of the PCM were washed away under extreme hemodynamics, and the detachment showed dependence on flow velocity, cell density and the time exposed to the flow. Increasing the cell density enhanced cellular resistance to flow, but typical changes in cell morphology and FAJ formation were no longer observed. Therefore, we established an optimal seeding density of 2×10^6 cells/cm^2 to maintain confluent cell layer for studying the glycocalyx and gene expression. Notably, the PCM tube diameter reaches 2.5 mm, which corresponds to the physiological diameter of the cephalic vein. This approach can be extended to larger diameters, even up to centimeter-scale models, by simply customizing the PCM to the corresponding size and fitting AVF model. However, according to the WSS calculation formula, maintaining the current WSS levels would require a significant increase in the inlet flow rate. Such high flow rates could introduce elevated pressures and impact forces that may damage the cellular layers on the PCM. Therefore, enhancing cell adhesion capabilities and improving the surface treatment of PCM will be essential to address these challenges effectively.

The flattened, retrievable PCM provided a 2D monolayer of cells that could be precisely mapped to disturbed flow hemodynamic profiles. While planar single-channel models remain the most common *in vitro* systems for studying flow effects on ECs, offering homogeneous cell exposure to stable or oscillatory shear stress, high cell yield for sampling, and direct imaging capability [38–40]. However, the lack of 3D vascular geometry impedes their replication of complex disturbed flow patterns at bifurcations configuration. 3D tubular models, typically fabricated by tunneling through hydrogels, avoid this limitation but are constrained to small diameters, hundreds of microns, to prevent wall deformation and enable full luminal imaging by microscopy [25,41,42]. However, such small-scale systems fail to reproduce large-vessel hemodynamics. To address this, some studies have employed millimeter-scale bifurcated tubes to mimic disturbed flow near vascular bifurcations [16,43]. Unfortunately, the increased curvature and diameter in these models impede high-resolution confocal imaging of the entire lumen which makes it impossible to precisely match hemodynamic profiles. Our study has resolved this trade-off through two key factors. Firstly, we used CFD as a robust method to predict the hemodynamics within the AVF model, effectively visualizing the distribution of hemodynamics on the tubular walls as contour plots and converting them into 2D images. The second key point is that the ultra-thin, plastic-retentive properties of the PCM prevent creasing during insertion, allowing it to regain its original flat state post-experiment while maintaining optical clarity for confocal microscopy. This methodological design conveniently aligns the 2D CFD images with specific point-to-point locations on tailored PCM, laying the groundwork for subsequent localization of four specific hemodynamic regions using confocal microscopy. This will facilitate precise verification of the influence of hemodynamics on cells within those regions in later studies. For specific regions on the membrane, confocal microscopy obtained high-resolution images at the subcellular level. With image stitching, we reconstructed the entire PCM surface (20×7.8 mm). The tailored PCM was manufactured to standardized dimensions, enabling precise coordinate registration within the confocal microscopy system, which permitted mathematical mapping of any point on the PCM to its corresponding CFD 2D contour coordinates. For analysis, we identified four representative hemodynamic regions on the CFD 2D contour plot, TAWSS MAX and TransWSS MAX on the outer wall, L/O on the inner wall and PF regions on the flow tract 10mm away from the anastomosis. The former three sites were 3mm within the anastomosis section and spaced at less than 2mm intervals with others. Our methodology enabled accurate localization of these regions on the PCM, facilitating targeted sampling of surrounding cells for phenotypic and molecular analysis, thereby eliminating microscopic sampling difficulties and overcoming the limitations of regional averaging in hemodynamic characterization.

Disturbed flow significantly affected the morphology and function of HUVECs on the outer and inner walls near the anastomosis. Under physiological hemodynamic conditions characterized by high TAWSS, low OSI/RRT, and unidirectional WSS vectors, ECs exhibit an atheroprotective phenotype. This includes flow-aligned elongation, stable AJs, elevated GLX expression, and increased levels of KLF2 and eNOS, collectively preserving barrier integrity and preventing IH. Conversely, disturbed flow conditions (low TAWSS, high OSI/RRT) triggered endothelial dysfunction, manifesting as cell rounding, loss of alignment, and a pro-inflammatory shift marked by elevated FAJs and reduced GLX, eNOS, and KLF2. These alterations ultimately caused cell barrier dysfunction and increased permeability [6,7,44–47]. Within the disturbed flow region, a WSS fixed point indicating the dramatic spatial variations in WSS magnitude and direction (near-zero TAWSS and WSS vector, max OSI and RRT) serves as a hotspot for IH. At this site, profound flow stagnation significantly prolongs particle residence time, facilitating atherogenic particle transportation in the vessel media [48,49]. The coexistence of this enhanced particle transport with a dysfunctional cellular barrier creates an environment highly conducive to IH initiation. Through CFD simulation and mapping of hemodynamic distribution to the PCM, this study found that the cells in the L/O region (low TAWSS, high OSI/RRT) performed a pro-inflammatory morphology and phenotype when compared to the PF region (high TAWSS, low OSI/RRT), these results are consistent with the understanding of the low and oscillatory WSS to the ECs found in the studies mentioned above, verifying our model can be used to study the effect of disturbed flow on endothelial cells. Notably, TAWSS MAX and TransWSS MAX on the outer wall, which characterized as relatively high but non-oscillatory WSS with perpendicular components, induced morphological changes similar to L/O regions with round cells and elevated FAJ. Though more GLX expressions were present on the outer wall than L/O, expression was reduced compared to PF. This contrasts with conventional cell responses under high and unidirectional WSS in the straight single-channel models, which promotes cell elongation and maintains barrier function. This discrepancy attributed to the complex hemodynamics near the bifurcation, where the outer wall experiences multidirectional WSS components—a finding consistent with reports that multidirectional WSS promotes coronary atherosclerosis [13]. Our results indicated that both high-magnitude oscillation and

high-magnitude multidirectionality can converge on a common pathway of endothelial dysfunction, explaining the elevated risk of IH at both the inner wall and specific sites on the outer wall. While the spatial overlap between the fixed point and the broader L/O region in our area-level model precludes attributing the observed effects solely to the fixed point, our PCM-matching methodology establishes a robust framework. This approach provides a viable pathway for future research to delineate the unique pathobiology at fixed points using single-cell or spatial omics.

The above findings suggested universal endothelial dysfunction at the AVF anastomosis, potentially predisposing to intimal hyperplasia. This aligns with clinical observations that the majority of the stenosis in radiocephalic AVFs were located at the juxta-anastomotic region [50, 51]. A study including 127 patients with swing segment AVF stenosis found that 63 % of the stenoses occurred 3 cm from the anastomosis [52]. Pathology revealed varying degrees of juxta-anastomotic intimal hyperplasia, with most samples showing eccentric hyperplasia [51,53]. While an animal study challenges the conventional view that IH occurs primarily on the inner wall due to the low and oscillatory WSS, this study demonstrated that disturbed flow firstly caused intimal endothelial denudation accompanied by thrombus formation at the venous outer wall facing the anastomosis. Eccentric and heterogenous neointimal hyperplasia formed under disturbed flow at the same location on the outer wall [54]. The high up-regulated PDGF/TGFβ gene expression on the outer walls was aligned with the previous study which showed the higher risk of IH on the outer wall. While prior studies reported L/O induced inflammatory markers, our 6-hour experiments detected no ICAM1/MCP1 changes across regions, possibly reflecting temporal dynamics of inflammatory responses. The location and mechanism of intimal hyperplasia in arteriovenous fistulas, as well as its relationship with hemodynamics, are currently unclear or even contradictory. With the emergence of spatial transcriptomics, it presents an unprecedented opportunity to synergize with our established hemodynamic-cellular mapping methodology. By correlating spatially resolved gene expression profiles with precisely mapped hemodynamic parameters, it may identify shear stress-responsive transcriptional programs and decode high-resolution endothelial mechanotransduction pathways. Such multidimensional analysis promises to reveal previously unrecognized relationships between complex flow patterns and spatially defined endothelial phenotypes at single-cell resolution.

In summary, this study developed an *in vitro* disturbed flow AVF model utilizing PCM as a cell carrier. This approach enables endothelial cell culture on the luminal surface, followed by post-experimental PCM flattening and computational registration with CFD coordinates. Through systematic analysis of cellular morphology, FAJ distribution, GLX coverage, and gene expression profiles, we have validated the differential effects of complex hemodynamics on endothelial cells near the anastomosis. This methodology establishes a robust framework bridging computational simulations with biological experimentation. However, several limitations should be acknowledged. Firstly, the non-standardized production of PCM membranes may introduce measurement variability in our experiments. Secondly, technical challenges persist regarding cell retention, particularly near the anastomosis under flow conditions. While increased cell density improves retention, it concurrently obscures morphological assessment. Conversely, reduced density compromises cell adherence. This density-dependent trade-off underscores the need for improved cell-seeding methodologies. Thirdly, while our modified Ibidi system improved upon static flow conditions, the inflow waveform (1 Hz, 6.11 cm/s peak velocity) lacks the spectral complexity of native arterial flow, particularly in its diastolic phase dynamics and harmonic content (e.g., absent dicrotic notch). This simplification may attenuate high-frequency WSS oscillations critical for endothelial mechanotransduction. Furthermore, the CFD simulations employed four key physiological simplifications: (1) rigid vessel walls, neglecting fluid-structure interactions (FSI) that may alter all wall dynamics *in-vivo*, especially in compliant venous segments; (2) pressure-free outflow boundary conditions that ignore downstream vascular resistance, potentially altering the flow split ratio and distribution near the anastomosis; (3) an idealized 60° bifurcation geometry that excludes anatomical variations in curvature and taper characteristic of human AVFs. (4) Furthermore, the CFD simulations assumed a Newtonian fluid, which, while a reasonable approximation for our xanthan gum-supplemented culture medium, does not capture the shear-thinning behavior of blood. This may lead to an overestimation of WSS in very low-shear regions in vivo. These assumptions enable controlled parametric studies; they limit direct translation of absolute WSS thresholds to clinical settings where patient-specific geometry and compliance dominate hemodynamics. The 24-hour experimental window may have also limited the expression of certain flow-induced genes or structural remodeling processes. Lastly, due to spatial proximity between distinct hemodynamic regions, gene expression analysis was performed on broader segments of the PCM (e.g., inner wall, outer wall), which may have masked finer gradients in shear-responsive transcriptional profiles.

CRediT authorship contribution statement

Zhuotao Xiao: Writing – original draft, Methodology, Formal analysis, Data curation, Conceptualization. **Nicholas A. White:** Writing – review & editing, Methodology, Conceptualization. **Jun Wen:** Writing – review & editing, Methodology, Conceptualization. **Rudmer J. Postma:** Writing – review & editing. **Wendy M.P.J. Sol:** Writing – review & editing, Methodology. **Bernard M. van den Berg:** Writing – review & editing, Methodology. **Anton Jan van Zonneveld:** Writing – review & editing. **Huybert J.F. van de Stadt:** Methodology. **Asad Mirza:** Writing – review & editing, Software, Methodology. **Roel Bijkerk:** Writing – review & editing. **Joris I. Rotmans:** Writing – review & editing, Supervision, Project administration, Methodology, Funding acquisition, Conceptualization.

Declaration of competing interest

The authors declare that they have no known competing financial interests or personal relationships that could have appeared to influence the work reported in this paper.

Acknowledgements

The authors acknowledge Light Microscopy Facility team of Leiden University Medical Center for co-ordinates mapping in confocal microscope. The authors acknowledge Wei Miu from Nanjing University of Science and Technology (China) for coding and MVNPE Precision Engineering (Netherlands) for manufacturing the AVF model. The model production was supported by Proefdiervrije, the Netherlands. This project was supported by Leiden University Medical Center and Zhuotao Xiao was supported by the China Scholarship Counsel [No. 202207720081].

Supplementary materials

Supplementary material associated with this article can be found, in the online version, at doi:10.1016/j.actbio.2026.01.044.

References

[1] A.A. Al-Jaishi, M.J. Oliver, S.M. Thomas, C.E. Lok, J.C. Zhang, A.X. Garg, S. D. Kosa, R.R. Quinn, L.M. Moist, Patency rates of the arteriovenous fistula for hemodialysis: a systematic review and meta-analysis, Am. J. Kidney Dis. 63 (3) (2014) 464–478.

[2] B. Ene-Iordache, A. Remuzzi, Disturbed flow in radial-cephalic arteriovenous fistulae for haemodialysis: low and oscillating shear stress locates the sites of stenosis, Nephrol. Dial. TransPlant 27 (1) (2012) 358–368.

[3] U. Morbiducci, A.M. Kok, B.R. Kwak, P.H. Stone, D.A. Steinman, J.J. Wentzel, Atherosclerosis at arterial bifurcations: evidence for the role of haemodynamics and geometry, Thromb. Haemost. 115 (3) (2016) 484–492.

[4] D.N. Ku, D.P. Giddens, C.K. Zarins, S. Glagov, Pulsatile flow and atherosclerosis in the human carotid bifurcation. Positive correlation between plaque location and low oscillating shear stress, Arteriosclerosis 5 (3) (1985) 293–302.
[5] P. Zhao, Q. Yao, P.J. Zhang, E. The, Y. Zhai, L. Ao, M.J. Jarrett, C.A. Dinarello, D. A. Fullerton, X. Meng, Single-cell RNA-seq reveals a critical role of novel pro-inflammatory EndMT in mediating adverse remodeling in coronary artery-on-a-chip, Sci. Adv. 7 (34) (2021).
[6] M. Mengistu, H. Brotzman, S. Ghadiali, L. Lowe-Krentz, Fluid shear stress-induced JNK activity leads to actin remodeling for cell alignment, J. Cell Physiol. 226 (1) (2011) 110–121.
[7] K.M. Parmar, H.B. Larman, G. Dai, Y. Zhang, E.T. Wang, S.N. Moorthy, J.R. Kratz, Z. Lin, M.K. Jain, M.A. Gimbrone Jr., G. García-Cardeña, Integration of flow-dependent endothelial phenotypes by Kruppel-like factor 2, J. Clin. Invest. 116 (1) (2006) 49–58.
[8] J.J. Chiu, S. Chien, Effects of disturbed flow on vascular endothelium: pathophysiological basis and clinical perspectives, Physiol. Rev. 91 (1) (2011) 327–387.
[9] H. Miao, Y.L. Hu, Y.T. Shiu, S. Yuan, Y. Zhao, R. Kaunas, Y. Wang, G. Jin, S. Usami, S. Chien, Effects of flow patterns on the localization and expression of VE-cadherin at vascular endothelial cell junctions: in vivo and in vitro investigations, J. Vasc. Res. 42 (1) (2005) 77–89.
[10] G. Dai, M.R. Kaazempur-Mofrad, S. Natarajan, Y. Zhang, S. Vaughn, B. R. Blackman, R.D. Kamm, G. García-Cardeña, M.A. Gimbrone Jr., Distinct endothelial phenotypes evoked by arterial waveforms derived from atherosclerosis-susceptible and -resistant regions of human vasculature, Proc. Natl. Acad. Sci. U S A 101 (41) (2004) 14871–14876.
[11] G. Wang, S. Kostidis, G.L. Tiemeier, W. Sol, M.R. de Vries, M. Giera, P. Carmeliet, B.M. van den Berg, T.J. Rabelink, Shear Stress Regulation of Endothelial Glycocalyx Structure Is Determined by Glucobiosynthesis, Arterioscler. Thromb. Vasc. Biol. 40 (2) (2020) 350–364.
[12] B. Ene-Iordache, C. Semperboni, G. Dubini, A. Remuzzi, Disturbed flow in a patient-specific arteriovenous fistula for hemodialysis: Multidirectional and reciprocating near-wall flow patterns, J. Biomech. 48 (10) (2015) 2195–2200.
[13] H.J. Carpenter, M.H. Ghayesh, A.C. Zander, P.J. Psaltis, On the nonlinear relationship between wall shear stress topology and multi-directionality in coronary atherosclerosis, Comput. Methods Programs Biomed. 231 (2023) 107418.
[14] M. Mohammed, P. Thurgood, C. Gilliam, N. Nguyen, E. Pirogova, K. Peter, K. Khoshmanesh, S. Baratchi, Studying the response of aortic endothelial cells under pulsatile flow using a compact microfluidic system, Anal. Chem. 91 (18) (2019) 12077–12084.
[15] Q. Ma, H. Ma, F. Xu, X. Wang, W. Sun, Microfluidics in cardiovascular disease research: state of the art and future outlook, Microsyst. Nanoeng. 7 (2021) 19.
[16] Z. Xiao, R.J. Postma, A.J. van Zonneveld, B.M. van den Berg, W. Sol, N.A. White, H. J.F. van de Stadt, A. Mirza, J. Wen, R. Bijkerk, J.I. Rotmans, A bypass flow model to study endothelial cell mechanotransduction across diverse flow environments, Mater. Today Bio 27 (2024) 101121.
[17] L. Antiga, M. Piccinelli, L. Botti, B. Ene-Iordache, A. Remuzzi, D.A. Steinman, An image-based modeling framework for patient-specific computational hemodynamics, Med. Biol. Eng. Comput. 46 (11) (2008) 1097–1112.
[18] G. Villa, S. Ringgaard, I. Hermann, R. Noble, P. Brambilla, D.S. Khatir, F.G. Zöllner, S.T. Francis, N.M. Selby, A. Remuzzi, A. Caroli, Phase-contrast magnetic resonance imaging to assess renal perfusion: a systematic review and statement paper, MAGMA 33 (1) (2020) 3–21.
[19] G. De Nisco, E.M.J. Hartman, E. Torta, J. Daemen, C. Chiastra, D. Gallo, U. Morbiducci, J.J. Wentzel, Predicting lipid-rich plaque progression in coronary arteries using multimodal imaging and wall shear stress signatures, Arterioscler. Thromb. Vasc. Biol. 44 (4) (2024) 976–986.
[20] E.M.J. Hartman, G. De Nisco, A.M. Kok, M. Tomaniak, F.M.A. Nous, S.A. Korteland, F.J.H. Gijsen, W.K. den Dekker, R. Diletti, N. van Mieghem, J.M. Wilschut, F. Zijlstra, A.F.W. van der Steen, R.P.J. Budde, J. Daemen, J.J. Wentzel, Wall shear stress-related plaque growth of lipid-rich plaques in human coronary arteries: an near-infrared spectroscopy and optical coherence tomography study, Cardiovasc. Res. 119 (4) (2023) 1021–1029.
[21] A. Hoogendoorn, A.M. Kok, E.M.J. Hartman, G. de Nisco, L. Casadonte, C. Chiastra, A. Coenen, S.A. Korteland, K. Van der Heiden, F.J.H. Gijsen, D.J. Duncker, A.F. W. van der Steen, J.J. Wentzel, Multidirectional wall shear stress promotes advanced coronary plaque development: comparing five shear stress metrics, Cardiovasc. Res. 116 (6) (2020) 1136–1146.
[22] A.A. Owida, H. Do, Y.S. Morsi, Numerical analysis of coronary artery bypass grafts: an over view, Comput. Methods Programs Biomed. 108 (2) (2012) 689–705.
[23] E.E. van Haaften, S. Quicken, W. Huberts, C.V.C. Bouten, N.A. Kurniawan, Computationally guided in-vitro vascular growth model reveals causal link between flow oscillations and disorganized neotissue, Commun. Biol. 4 (1) (2021) 546.
[24] D. Vreeken, C.S. Bruikman, S.M.L. Cox, H. Zhang, R. Lalai, A. Koudijs, A.J. van Zonneveld, G.K. Hovingh, J.M. van Gils, EPH receptor B2 stimulates human monocyte adhesion and migration independently of its EphrinB ligands, J. Leukoc. Biol. 108 (3) (2020) 999–1011.
[25] M. Bulut, M. Vila Cuenca, M. de Graaf, F.E. van den Hil, C.L. Mummery, V. V. Orlova, Three-dimensional Vessels-on-a-Chip Based on hiPSC-derived vascular endothelial and smooth muscle cells, Curr. Protoc. 2 (10) (2022) e564.
[26] J.H. Ryu, P.B. Messersmith, H. Lee, Polydopamine surface chemistry: a decade of discovery, ACS Appl. Mater. Interfaces. 10 (9) (2018) 7523–7540.
[27] P. Baranowska, M. Kopińska, D. Kołodziejek, E. Jastrzębska, Z. Brzózka, Microfluidic system for generating a three-dimensional (3D) vascularized islet-on-a-chip model, Sensors and Actuators B: Chem. 418 (2024) 136302.
[28] C.N. van den Broek, R.A. Pullens, O. Frøbert, M.C. Rutten, W.F. den Hartog, F. N. van de Vosse, Medium with blood-analog mechanical properties for cardiovascular tissue culturing, Biorheology 45 (6) (2008) 651–661.
[29] P. Rangamani, A. Lipshtat, E.U. Azeloglu, R.C. Calizo, M. Hu, S. Ghassemi, J. Hone, S. Scarlata, S.R. Neves, R. Iyengar, Decoding information in cell shape, Cell 154 (6) (2013) 1356–1369.
[30] S. Huveneers, J. Oldenburg, E. Spanjaard, G. van der Krogt, I. Grigoriev, A. Akhmanova, H. Rehmann, J. de Rooij, Vinculin associates with endothelial VE-cadherin junctions to control force-dependent remodeling, J. Cell Biol. 196 (5) (2012) 641–652.
[31] J. Schindelin, I. Arganda-Carreras, E. Frise, V. Kaynig, M. Longair, T. Pietzsch, S. Preibisch, C. Rueden, S. Saalfeld, B. Schmid, J.Y. Tinevez, D.J. White, V. Hartenstein, K. Eliceiri, P. Tomancak, A. Cardona, an open-source platform for biological-image analysis, Nat. Methods 9 (7) (2012) 676–682.
[32] I.C. Harding, R. Mitra, S.A. Mensah, I.M. Herman, E.E. Ebong, Pro-atherosclerotic disturbed flow disrupts caveolin-1 expression, localization, and function via glycocalyx degradation, J. Transl. Med. 16 (1) (2018) 364.
[33] M.G. Boels, M.C. Avramut, A. Koudijs, M.J. Dane, D.H. Lee, J. van der Vlag, A. J. Koster, A.J. van Zonneveld, E. van Faassen, H.J. Gröne, B.M. van den Berg, T. J. Rabelink, Atrasentan reduces albuminuria by restoring the glomerular endothelial glycocalyx barrier in diabetic nephropathy, Diabetes 65 (8) (2016) 2429–2439.
[34] L. Yuan, S. Cheng, W. Sol, A.I.M. van der Velden, H. Vink, T.J. Rabelink, B.M. van den Berg, Heparan sulfate mimetic fucoidan restores the endothelial glycocalyx and protects against dysfunction induced by serum of COVID-19 patients in the intensive care unit, ERJ. Open. Res. 8 (2) (2022).
[35] M. Hu, Y. Li, J. Huang, X. Wang, J. Han, Electrospun scaffold for biomimic culture of Caco-2 cell monolayer as an in vitro intestinal model, ACS Appl. Bio Mater. 4 (2) (2021) 1340–1349.
[36] R. Sharif, B. Fowler, D. Karamichos, Collagen cross-linking impact on keratoconus extracellular matrix, PLoS One 13 (7) (2018) e0200704.
[37] A. Rizzo, C. Vasco, V. Girgenti, V. Fugnanesi, C. Calatozzolo, A. Canazza, A. Salmaggi, L. Rivoltini, M. Morbin, E. Ciusani, Melanoma cells homing to the brain: an in vitro model, Biomed. Res. Int. 2015 (2015) 476069.
[38] S.G. Hong, J.W. Ashby, J.P. Kennelly, M. Wu, M. Steel, E. Chattopadhyay, R. Foreman, P. Tontonoz, E.J. Tarling, P. Turowski, M. Gallagher-Jones, J.J. Mack, Mechanosensitive membrane domains regulate calcium entry in arterial endothelial cells to protect against inflammation, J. Clin. Invest. 134 (13) (2024).
[39] S.G. Hong, J.P. Kennelly, K.J. Williams, S.J. Bensinger, J.J. Mack, Flow-mediated modulation of the endothelial cell lipidome, Front. Physiol. 15 (2024) 1431847.
[40] J. Jatzlau, P.L. Mendez, A. Altay, L. Raaz, Y. Zhang, S. Mähr, A. Sesver, M. Reichenbach, S. Mundlos, M. Vingron, P. Knaus, Fluid shear stress-modulated chromatin accessibility reveals the mechano-dependency of endothelial SMAD1/5-mediated gene transcription, iScience 26 (9) (2023) 107405.
[41] J.S. Choi, T.S. Seo, Orthogonal co-cultivation of smooth muscle cell and endothelial cell layers to construct in vivo-like vasculature, Biomicrofluidics 13 (1) (2019) 014115.
[42] C. Mandrycky, B. Hadland, Y. Zheng, 3D curvature-instructed endothelial flow response and tissue vascularization, Sci. Adv. 6 (38) (2020).
[43] G. Gao, P. Wonbin, B. Kim, M. Ahn, S. Chae, W.W. Cho, J. Kim, J.Y. Lee, J. Jang, Construction of a novel in vitro atherosclerotic model from geometry-tunable artery equivalents engineered via in-bath coaxial cell printing, Adv. Funct. Mater. 31 (2020) 2008878.
[44] W. Meng, M. Takeichi, Adherens junction: molecular architecture and regulation, Cold. Spring. Harb. Perspect. Biol. 1 (6) (2009) a002899.
[45] L. He, C.L. Zhang, Q. Chen, L. Wang, Y. Huang, Endothelial shear stress signal transduction and atherogenesis: From mechanisms to therapeutics, Pharmacol. Ther. 235 (2022) 108152.
[46] M. Gouverneur, J.A. Spaan, H. Pannekoek, R.D. Fontijn, H. Vink, Fluid shear stress stimulates incorporation of hyaluronan into endothelial cell glycocalyx, Am. J. Physiol. Heart. Circ. Physiol. 290 (1) (2006) H458. -2.
[47] R. Mitra, J. Qiao, S. Madhavan, G.L. O'Neil, B. Ritchie, P. Kulkarni, S. Sridhar, A. L. van de Ven, E.M.C. Kemmerling, C. Ferris, J.A. Hamilton, E.E. Ebong, The comparative effects of high fat diet or disturbed blood flow on glycocalyx integrity and vascular inflammation, Transl. Med. Commun. 3 (2018).
[48] A. Arzani, S.C. Shadden, Wall shear stress fixed points in cardiovascular fluid mechanics, J. Biomech. 73 (2018) 145–152.
[49] J.L. Zhao, L. Jia, X.B. Wang, L.L. Zhang, M.H. Li, Effects of adjustable impinging flow on the vascular endothelial cell layer in a modified T chamber, (2017).
[50] K. Hu, Y. Guo, Y. Li, C. Lu, C. Cai, S. Zhou, Z. Ke, Y. Li, W. Wang, Oxidative stress: An essential factor in the process of arteriovenous fistula failure, Front. Cardiovasc. Med. 9 (2022) 984472.
[51] K.B. Quencer, M. Arici, Arteriovenous Fistulas and Their Characteristic Sites of Stenosis, AJR Am. J. Roentgenol. 205 (4) (2015) 726–734.
[52] O.J. Badero, M.O. Salifu, H. Wasse, J. Work, Frequency of swing-segment stenosis in referred dialysis patients with angiographically documented lesions, Am. J. Kidney Dis. 51 (1) (2008) 93–98.
[53] O.K. Jahrome, I. Hoefer, G.J. Houston, P.A. Stonebridge, P.J. Blankestijn, F.L. Moll, G.J. de Borst, Hemodynamic effects of spiral ePTFE prosthesis compared with standard arteriovenous graft in a carotid to jugular vein porcine model, J. Vasc. Access. 12 (3) (2011) 224–230.
[54] H. Bai, Z. Li, W. Zhang, C. Thaxton, Y. Ohashi, L. Gonzalez, M. Kano, B. Yatsula, J. Hwa, A. Dardik, Early thrombus formation is required for eccentric and heterogeneous neointimal hyperplasia under disturbed flow, J. Thromb. Haemost. 22 (12) (2024) 3614–3628.